

# 3D meshes of carbon nanotubes guide functional reconnection of segregated spinal explants

Sadaf Usmani,<sup>1\*</sup> Emily Rose Aurand,<sup>2\*</sup> Manuela Medelin,<sup>2</sup> Alessandra Fabbro,<sup>2</sup> Denis Scaini,<sup>2,3</sup> Jummi Laishram,<sup>2</sup> Federica B. Rosselli,<sup>1</sup> Alessio Ansuini,<sup>1</sup> Davide Zoccolan,<sup>1</sup> Manuela Scarselli,<sup>4</sup> Maurizio De Crescenzi,<sup>4</sup> Susanna Bosi,<sup>5</sup> Maurizio Prato,<sup>5,6,7†</sup> Laura Ballerini<sup>1†</sup>

2016 © The Authors, some rights reserved; exclusive licensee American Association for the Advancement of Science. Distributed under a Creative Commons Attribution NonCommercial License 4.0 (CC BY-NC). 10.1126/sciadv.1600087

In modern neuroscience, significant progress in developing structural scaffolds integrated with the brain is provided by the increasing use of nanomaterials. We show that a multiwalled carbon nanotube self-standing framework, consisting of a three-dimensional (3D) mesh of interconnected, conductive, pure carbon nanotubes, can guide the formation of neural webs in vitro where the spontaneous regrowth of neurite bundles is molded into a dense random net. This morphology of the fiber regrowth shaped by the 3D structure supports the successful reconnection of segregated spinal cord segments. We further observed in vivo the adaptability of these 3D devices in a healthy physiological environment. Our study shows that 3D artificial scaffolds may drive local rewiring in vitro and hold great potential for the development of future in vivo interfaces.

## INTRODUCTION

Multimodal neuronal prostheses of the future will combine tissue engineering with electrical interfacing technologies to develop neurohybrid microsystems capable of improving the innate capacity of the central nervous system (CNS) to recover or rehabilitate lost functions (1–4). Despite obvious difficulties, implantable devices hold tremendous promise to overcoming the effects of CNS lesions and diseases. Nanotechnology enters this arena by developing new generations of nanomaterials to interface neuronal network formation and signaling with unprecedented abilities (5). In particular, carbon-based nanostructures, such as multiwalled carbon nanotubes (MWCNTs), have great potential for neurological applications, featuring dimensions and properties reminiscent of specific compartments of the neural machinery, and have already been shown to govern in vitro synapse formation, cell excitability, and synaptic processing (6–12). The precise biophysical mechanisms of these special interactions between MWCNTs and neurons are not completely understood (6, 7). However, the features and the remarkable applications of such materials (13), together with their ability to manipulate neural activity, hold strong promise in manufacturing interfaces enriched by artificial environmental cues that can guide tissue reconstruction. The transition from being two-dimensional (2D) to becoming 3D in such MWCNT constructs may open new horizons in treating injured CNS tissues, such as the spinal cord. In implant technology, the design of electroactive scaffolds has been exploited to support electrical interactions within neuronal cell networks and to improve guided tissue regeneration (14–16). An additional study reported that soluble functionalized carbon nanotubes may exert potential benefits when administered in the lesioned spinal cord, representing a promising substrate for scaffolding (17); however, the potential impact of pure carbon nanotubes when used as scaffolds has not been explored. Here, we test the ability of MWCNT-based 3D

structures to dictate neurite web morphology toward successful reconnection of segregated spinal explants in vitro. By confocal microscopy, we address the ability of 3D MWCNT to design the geometry of the newly formed neural nets. By means of electrophysiology, we address to what extent these 3D MWCNT-neurite structures promote the synchronization of rhythmic outputs generated by separated spinal explants. In addition, we report, for the first time, the tissue reaction and glial scar formation upon in vivo implantation of these materials.

## RESULTS AND DISCUSSION

We have previously characterized, in vitro, the ability of MWCNT 2D layers to support neuronal growth and synapse formation (6–11). To investigate the potential ability of these nanomaterials to guide CNS network reorganization in 3D, we manufactured self-standing 3D meshes of interconnected MWCNTs (Fig. 1A). These structures were interfaced in vitro with long-term, cocultured pairs of mouse organotypic spinal cord explants that allow the development of spinal networks over extended periods (18–21). Cocultured transverse slices were separated by a distance known to impair their functional reconnection under basal conditions (>300  $\mu\text{m}$ ) (18) and represent an efficient experimental paradigm to test the effectiveness of spontaneous regeneration of intrinsic interneuron projections (18) in recovering coherent motor outputs (22). Control slices (Controls) were grown embedded in a gelified protein-rich plasma clot (that is, fibrin glue; average distance among the two slices,  $1.91 \pm 0.50$  mm;  $n = 40$  slices), whereas those supported by the 3D carbon nanotube frame (3D CNF) were interfaced with the 3D MWCNT structures and included in the same plasma gel (average slice distance,  $1.63 \pm 0.42$  mm;  $n = 36$  slices; not significantly different from Controls,  $P = 0.08$ ).

### 3D microsystems reconnecting segregated spinal explants

Spinal organotypic slices upon >2 weeks of culturing exhibit a characteristic outgrowth of nerve fibers (8, 21) in both groups (highlighted in Fig. 1B). We explore the patterns of growth by randomly acquiring visual fields (28 and 30 fields,  $n = 9$  and  $n = 11$ , for Control and 3D CNF, respectively) via confocal microscopy, where  $\beta$ -tubulin III-positive or SMI-32-positive processes surrounding the slice explants were

<sup>1</sup>International School for Advanced Studies (SISSA/ISAS), Trieste 34136, Italy. <sup>2</sup>Department of Life Sciences, University of Trieste, Trieste 34127, Italy. <sup>3</sup>NanoInnovation Laboratory, ELETTRA Synchrotron Light Source, Trieste 34149, Italy. <sup>4</sup>Department of Physics, University of Rome Tor Vergata, Rome 00173, Italy. <sup>5</sup>Department of Chemical and Pharmaceutical Sciences, University of Trieste, Trieste 34127, Italy. <sup>6</sup>Carbon Nanotechnology Laboratory, CIC biomaGUNE, Paseo de Miramón 182, 20009 Donostia-San Sebastián, Spain. <sup>7</sup>Ikerbasque, Basque Foundation for Science, 48013 Bilbao, Spain. \*These authors contributed equally to this work.

†Corresponding author. Email: laura.ballerini@sisssa.it (L.B.); prato@units.it (M.P.)

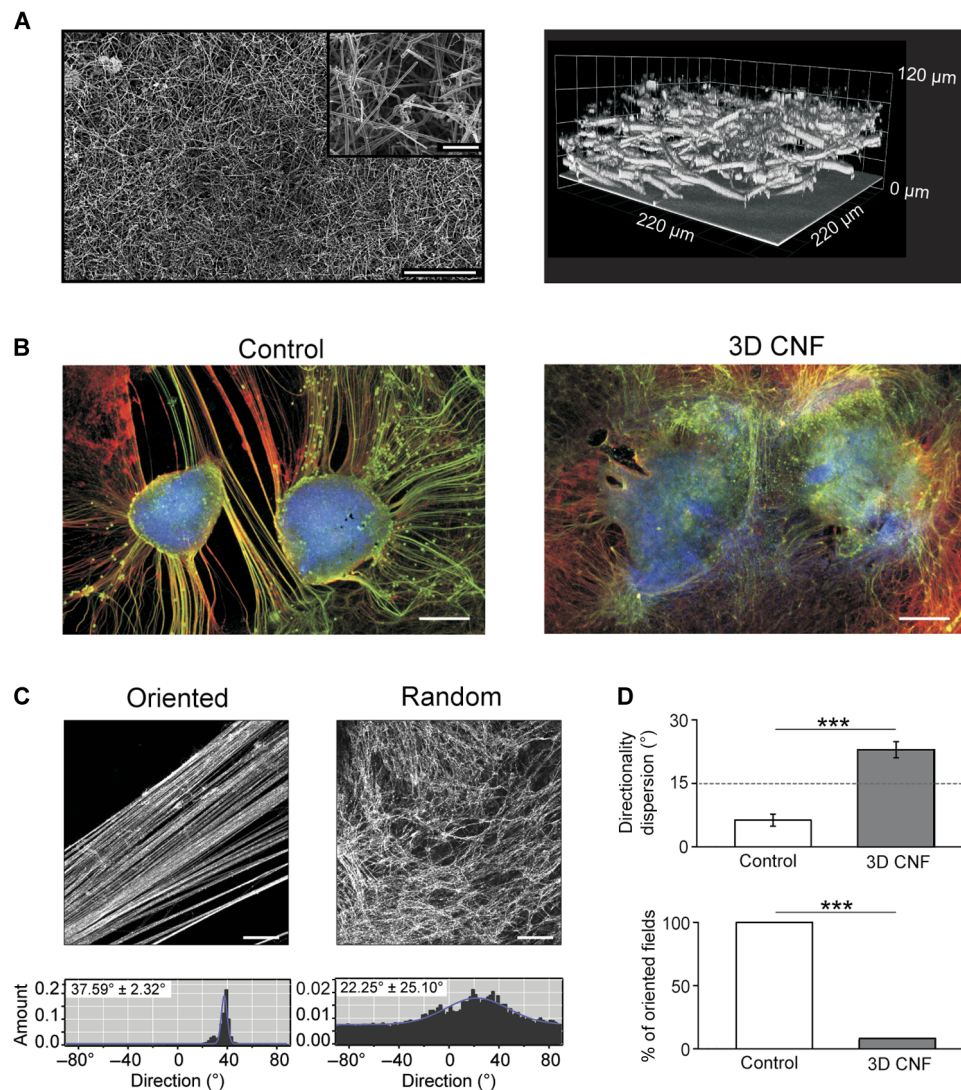


**Fig. 1. 3D CNF scaffolds redirect neurite outgrowth between spinal organotypic slices.** (A) SEM micrographs (left) of 3D CNF. At higher magnification (inset), the random skeleton of interconnected MWCNTs is shown. Confocal 3D reconstruction (right; reflection mode) of the same CNF scaffold. (B) Spinal slices cocultured in Control and in 3D CNF after 14 days of growth. Immunofluorescence is for neuron-specific microtubules ( $\beta$ -tubulin III; red), neurofilament H (SMI-32; green), and nuclei [4',6-diamidino-2-phenylindole (DAPI); blue]. (C) Confocal micrographs showing  $\beta$ -tubulin III-positive neuronal projection appearance in Control (oriented; left) and in 3D CNF (random; right) and the corresponding plots (bottom) of fiber angle direction distribution. In the example, oriented field fibers are characterized by a mean directionality value of  $37.6^\circ$  and a dispersion value of  $2.3^\circ$ , whereas random field fibers show values of  $22.3^\circ$  and  $25.1^\circ$ , respectively (values evaluated from the Gaussian fitting; see Materials and Methods). (D) Top histograms summarize the mean values of fiber orientation dispersion in Control and 3D CNF ( $***P < 0.001$ ); bottom histograms depict the percentage of visual fields in which fibers are aligned with a degree of dispersion less than  $15^\circ$ . In Controls, all samples (100%) contained oriented fibers with less than  $15^\circ$  of dispersion, whereas 7% of 3D CNF contained fibers with less than  $15^\circ$  of dispersion ( $***P < 0.001$ ). Scale bars, 250 and 25  $\mu\text{m}$  (inset) (A), 500  $\mu\text{m}$  (B), and 100  $\mu\text{m}$  (C).

visualized. In Controls, as previously reported (8), the outgrowth of neuronal projections was typically organized into thick bundles of aligned fibers [Fig. 1C (top left) and fig. S4A]. In contrast, the support of 3D CNF shaped the morphology of neurites outgrowing from the spinal explants into a complex web of randomly oriented processes [Fig. 1C (top right) and fig. S4B] invading the scaffold into the third dimension (see below). By fiber directionality analysis (23), we measured the dispersion of the mean fiber's direction in the two groups (see examples in fig. S4). Figure 1C (bottom) shows sample histograms plotting the angular distribution of the detected

structures. In these plots, the Gaussian fitting shows a narrow peak (left) in the presence of small directionality dispersion, indicating clear fiber orientation; conversely, the Gaussian fitting shows a broader distribution (right) indicating randomly oriented fibers (see Materials and Methods). Figure 1D top histograms summarize these results for Controls and 3D CNF [note the significant difference ( $P < 0.001$ ) in the directionality dispersion values]. We quantified the percentage of fields containing aligned oriented fibers, defined as fields showing mean directionality dispersion lower than  $15^\circ$  (see Materials and Methods). These results are summarized in the bar plot of Fig. 1D (bottom), which

shows that the occurrence of oriented fields was significantly reduced in 3D CNF ( $\chi^2 = 23.26$ ,  $P = 0.000001$ ; see the Supplementary Materials).

To explore whether the neuronal processes followed the third dimension of the scaffold in 3D CNF, we reconstructed 3D images from confocal Z stacks (Fig. 2A). The neurite networks emerging from spinal slices on the 3D MWCNTs are reconstructed in the confocal rendering in Fig. 2B, whereas Fig. 2C shows a scanning electron microscopy (SEM) snapshot of the hybrid web, where the MWCNT's mesh is nearly paralleled by the morphology of the neuronal fibers. We directly

compared webs of  $\beta$ -tubulin III-positive and SMI-32-positive processes from Control and 3D CNF and found that the depth of the neuronal process networks was significantly greater ( $P < 0.05$ ) with the 3D CNF, demonstrating that the neurites from the spinal slices are populating the third dimension of the nanoscaffold (for  $\beta$ -tubulin III-positive processes: Control,  $19 \pm 6 \mu\text{m}$  in  $n = 9$  visual fields; 3D CNF,  $49 \pm 33 \mu\text{m}$  in  $n = 14$  visual fields; for SMI-32-positive processes: Control,  $18 \pm 6 \mu\text{m}$  in  $n = 9$  visual fields; 3D CNF,  $38 \pm 20 \mu\text{m}$  in  $n = 14$  visual fields; Fig. 2, D and E).

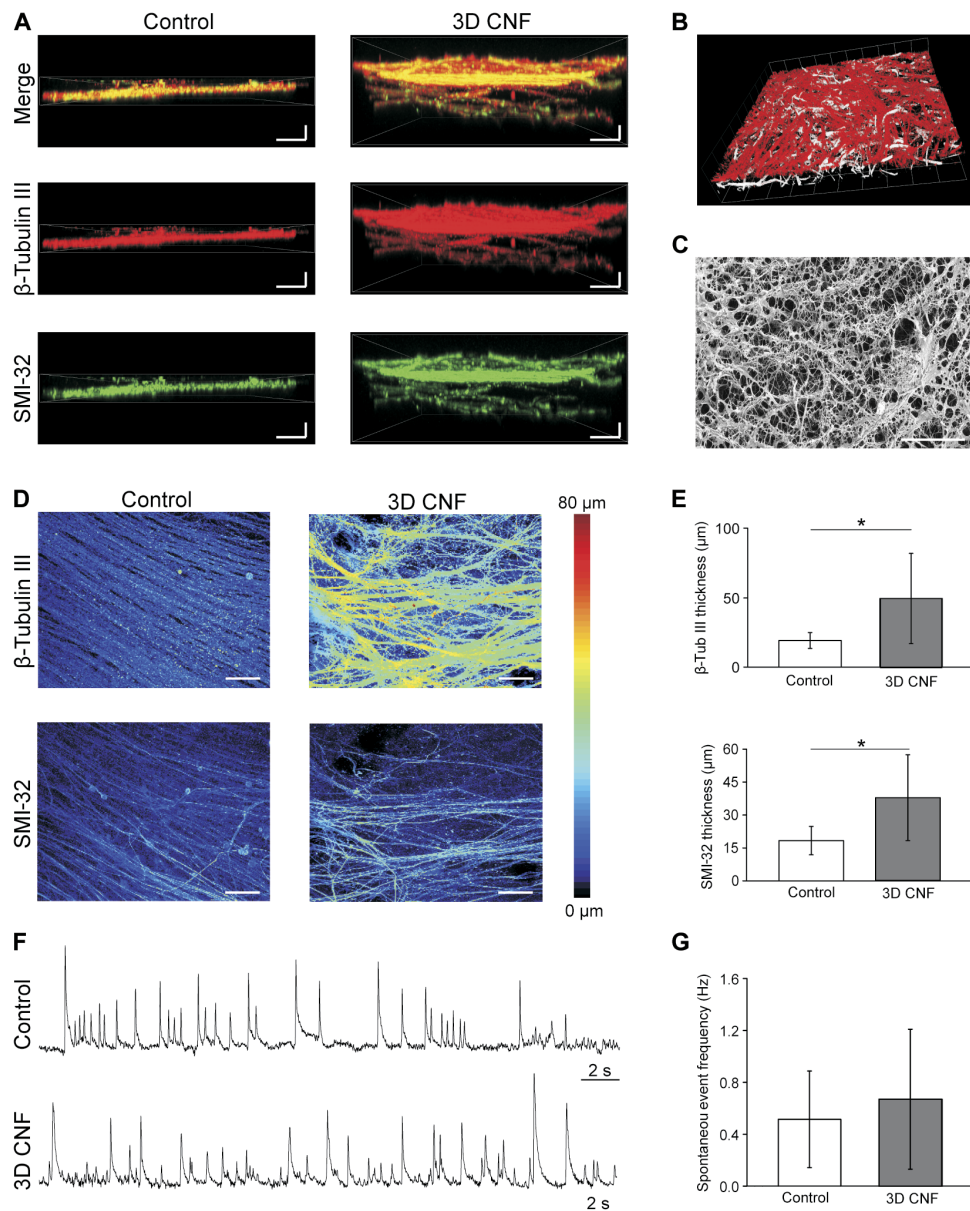


**Fig. 2. 3D CNF favors neuronal process paths in the third dimension.** (A) Detailed Z stack distribution of neuronal processes. Control neuronal processes are compared to 3D CNF ones by confocal microscopy. (B) Tilted confocal reconstruction of the intricate network of 3D CNF (white) and neuronal projections ( $\beta$ -tubulin III; red) (note the emergence of a 3D hybrid network knitted by the neuronal processes and the MWCNTs). (C) SEM micrograph of the hybrid network [same sample as in (B)]. (D) Volume rendering of the Z stacks of the neuronal processes in Control and 3D CNF samples. Neuronal processes under control conditions are relatively flat, whereas processes form a thicker layer when supported by 3D CNF. (E) Plots quantify the thicknesses of  $\beta$ -tubulin III-positive and SMI-32-positive processes ( $*P < 0.05$ , Student's t test). (F) Spontaneous LFPs recorded in Control and 3D CNF. (G) Spontaneous LFP mean frequencies. Scale bars, 25  $\mu\text{m}$  (horizontal) and 10  $\mu\text{m}$  (vertical) (A), 40  $\mu\text{m}$  (C), and 25  $\mu\text{m}$  (D).

Cultured spinal explants display prominent spontaneous electrical activity (8, 24–27). We monitored ventrally recorded extracellular potentials [local field potentials (LFPs)] to gain insights into the function of premotor circuits under the two growth conditions. Figure 2F shows sample tracings of spontaneous LFPs detected from Control and 3D CNF slices. When we analyzed 15 organotypic cocultures ( $n = 8$  Control and  $n = 7$  3D CNF; four different culture series; Fig. 2, F and G), the voltage tracings displayed similar LFP frequency ( $0.51 \pm 0.37$  and  $0.67 \pm 0.54$  Hz, respectively;  $P = 0.52$ ), confirming that 3D CNF favors the usual spinal network growth and maturation.

Simultaneous recordings of ventral LFPs were performed from the two cocultured spinal slices in both groups (sketched in Fig. 3A) to assess the presence of synchronous ventral outputs (18). To examine the functional consequences of the different patterns of projections in Control and 3D CNF ( $n = 16$  culture series), we used the glycine/ $\gamma$ -aminobutyric acid type A receptor antagonists strychnine (1  $\mu$ M) and bicuculline (20  $\mu$ M) to weaken synaptic inhibition. As previously reported for the entire spinal cord (27) and organotypic spinal slices (20, 24), the weakening of inhibition induced a switch from random bursting to synchrony, leading to the appearance of slow-paced bursting in the cocultured explants in all cultures tested (Fig. 3B, sample tracings for Control and 3D CNF). The bursting frequency, quantified as interevent interval, was similar in Control and 3D CNF ( $14.5 \pm 6.3$  and  $16.5 \pm 8.8$  s,  $n = 8$  and  $n = 14$ , respectively;  $P = 0.60$ ). The functional connectivity between the two slices was assessed by cross-correlation analysis of the disinhibited bursting. In Control, only 27% (6 of 22 pairs) of the cocultured explants were correlated, displaying a Pearson correlation coefficient (CCF) that was significantly larger than that expected by chance (see the Supplementary Materials and fig. S1), whereas the mean CCF was  $0.25 \pm 0.22$  ( $n = 22$ ; Fig. 3, C and D). In 17 Controls, stimulating (0.05 to 0.2 Hz) the dorsal region (Fig. 3, E and F) of one explant entrained the disinhibited rhythm of the same explant, but only a minority (29%; 5 of 17 pairs) succeeded in entraining (mean latency,  $118 \pm 92$  ms) the nonstimulated slice (cross-entrainment; Fig. 3G); this result did not change when the stimulation was moved to the contralateral slice. Together, these data indicate that only in a minority of Controls was there successful reconnection of the two cocultured explants, despite the huge outgrowth of fibers (8, 21).

On the contrary, in 3D CNF, the mean CCF value was  $0.56 \pm 0.27$  ( $n = 17$ ), which was significantly different from the Control (Fig. 3C;  $P < 0.001$ ), and correlated activity of disinhibited bursting between the two explants was observed in 94% of cases (16 of 17 pairs; see the Supplementary Materials and fig. S1), a fraction that was significantly larger than what was observed for the Control (Fig. 3D;  $\chi^2 = 16.56$ ,  $P < 0.001$ ). Because distance is a relevant variable (18), it is important to note that, within the range of distances analyzed, the CCF values of correlated pairs were not positively correlated ( $r = -0.271$ ,  $P = 0.31$ ) with the interslice distance variability, as reported in fig. S1D. Furthermore, when stimulating the dorsal area of one slice, cross-entrainment (mean latency,  $156 \pm 84$  ms; a value that was not significantly different from Controls,  $P = 0.448$ ) between explants was present in 10 of 13 pairs (that is, in 77% of cases; Fig. 3, F and G) and was also present when changing the stimulated slice within a given pair. In both groups, the emergence of functional coupling was unrelated to age in culture (Fig. 3H; note that blue symbols indicate functional correlated pairs measured as described in the Supplementary Materials and fig. S1).

To assess the impact of promoting 3D growth of fibers in the absence of MWCNTs, we next challenged cocultured pairs of spinal

slices with polydimethylsiloxane (PDMS)-based 3D porous structures (3D-PDMS) (28) ( $n = 5$ ; fig. S2). 3D-PDMS scaffolds are characterized by micropores of irregular shapes and dimensions interconnected with random paths of connectivity and were shown to implement 3D neurite's growth (28). In 3D-PDMS-cocultured spinal slices, the outgrowing  $\beta$ -tubulin III-positive fibers successfully infiltrated the structure in the third dimension (fig. S2A). However, 3D-PDMS samples displayed a mean value of the angular distribution of fibers (fig. S2C) and a value of the fraction of correlated pairs (fig. S2F) that were not significantly different ( $P = 0.24$  and  $P = 0.68$ , respectively) from Controls ( $n = 7$ ; fig. S2F). In a parallel approach, we tested 2D MWCNT substrates (8) to isolate the impact of MWCNTs per se in reestablishing an effective connectivity (fig. S2B;  $n = 7$ ). MWCNTs were reported to affect spinal slices (8); however, in cocultured explants, the fraction of correlated pairs did not significantly differ ( $P = 0.58$ ) from Controls (fig. S2F). Morphological analysis of the explants outgrowing fibers revealed that in 2D MWCNTs, the angular distribution displayed a significantly higher ( $P = 0.008$ ) dispersion when compared to Controls (fig. S2C). In the attempt to quantify the amount of fibers outgrowing the spinal slices under the different conditions, we measured the percentage of area of  $\beta$ -tubulin III-positive processes. As depicted in the bar plot of fig. S2D, we found a significantly increased [one-way analysis of variance (ANOVA),  $F_{3,38} = 3.99$ ,  $P = 0.015$ ]  $\beta$ -tubulin III-positive fluorescence area in 2D MWCNTs ( $P = 0.011$ ) and 3D CNF ( $P = 0.004$ ), suggesting that the high dispersion of fibers results in higher area values when slices are interfaced with 2D or 3D carbon nanotubes. We have previously reported that 2D MWCNTs improve the regrowth of neurites' bundles when interfaced with single spinal explants (8); however, it is difficult to consistently document a similar improvement in 3D CNF. The 3D regrowth implies a different volume distribution of the neurites. Ultimately, comparing thick fasciculation of processes in 2D with the outgrowth of dispersed 3D fibers in CNF renders these data inconclusive.

The morphological analysis of the four growth conditions suggests that crucial to the effects of 3D CNF is the ability of these scaffolds to guide the 3D random morphology of outgrowing neurites in the third dimension, because the improved directionality dispersion and the amount of  $\beta$ -tubulin III-positive area brought about by 2D MWCNT are insufficient to significantly improve the fraction of correlated pairs. Alternatively, the conductive scaffold may mediate a direct electrical transmission between cultured slices; however, this seems to be excluded by the entrainment testing, where we detected comparable values of latencies in stimulated coupled slices between 3D CNF and Controls. The measured latency values agree with the reported intersegmental delays in the entire spinal cord (29) and may indicate the presence of multisynaptic pathways in guiding the functional reconnection of the explanted segments. Thus, 3D CNF restores and/or reinforces the functional coupling among artificially separated spinal slices when compared to fibrin glue alone, and these effects are not reproduced by 3D-PDMS or 2D MWCNTs when tested separately. The interactions among the numerous physical, chemical, and biological factors translating the exposure to 3D MWCNTs into axonal regrowth, synapse formation, and extracellular matrix deposition along with the coculture growth in vitro are not further addressed in the current study, all of these being potential factors that could enable proper synapse formation and reconstruct functional bridges among severed networks (30). Nevertheless, it is tempting to speculate that destructuring fiber fasciculation by a 3D template of carbon nanotubes may contribute to the functional reconnection of separated spinal slices, leading to an improved synchrony of rhythmic outputs.

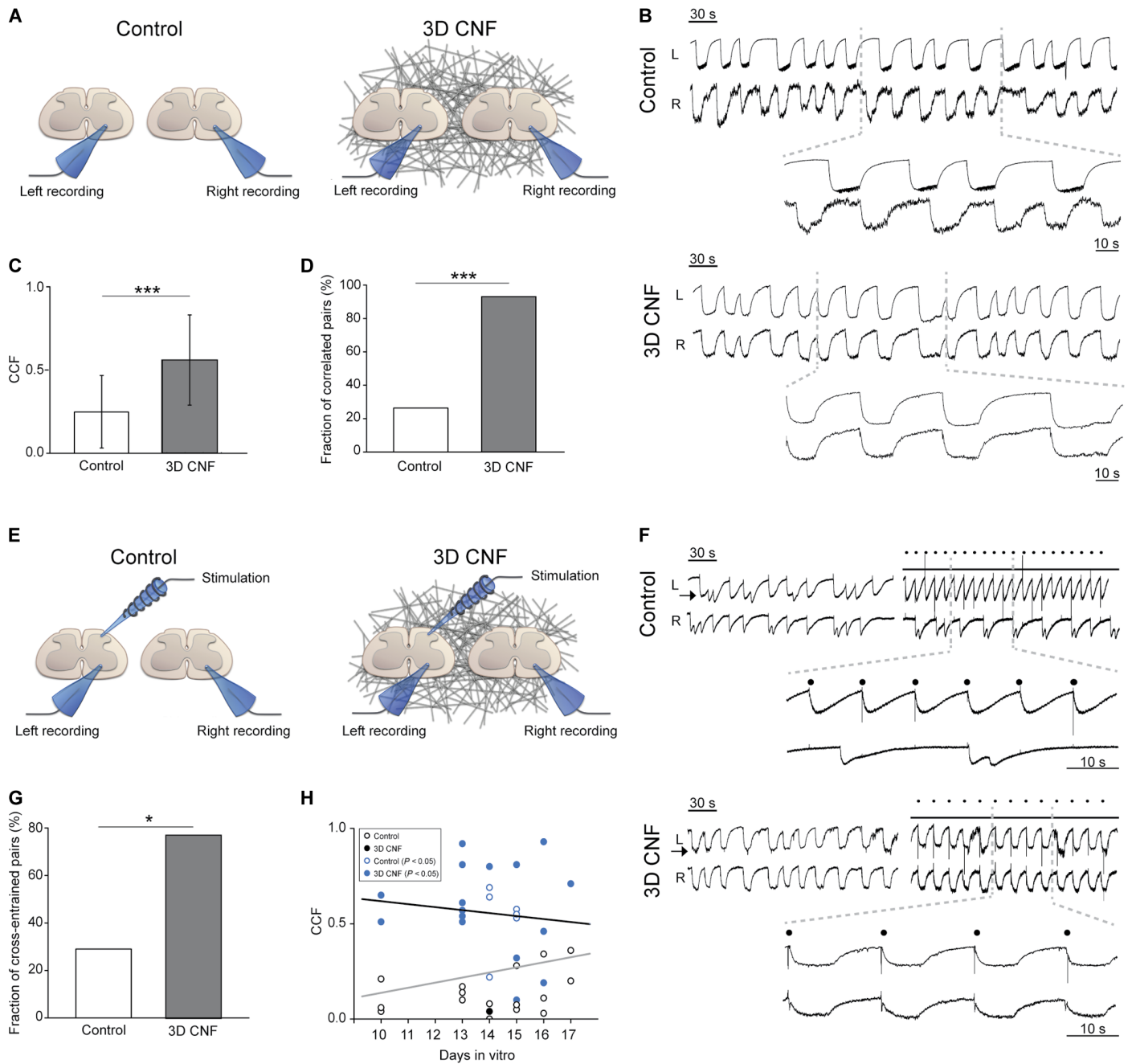


**Fig. 3. 3D CNF guides the functional reconnection of ventral outputs in segregated spinal organotypic slices.** (A) Sketch of the experimental setting for double-slice ventral recordings. (B) LFP bursting induced by strychnine and bicuculline recorded simultaneously from left (L) and right (R) slices in Control and 3D CNF. Right insets are the corresponding cross-correlation plots. (C) Average CCF from Control and 3D CNF (\*\*\* $P < 0.001$ ). (D) The fraction of spinal explants that were significantly correlated is significantly larger in 3D CNF (\*\*\* $P < 0.001$ ,  $\chi^2$  test). (E) Sketch of the experimental setting for dorsal stimulation. (F) Bursting LFP entrainment by dorsal electrical stimulation (dots) of left slices (arrow) in Control and 3D CNF slice pairs (note 3D CNF premotor output entrainment in both slices). (G) 3D CNF increases the fraction of cross-entrained explants (\* $P < 0.05$ ,  $\chi^2$  test). (H) Age in vitro is not correlated with CCF values (gray and black lines: regression lines for Control and 3D CNF conditions,  $r = 0.249$  and  $-0.113$ , respectively; blue open and filled circles highlight significant correlated pairs).

### Biocompatibility of 3D CNF implanted in vivo

In vitro 3D CNF was invaded by regrowing fibers, and we suggest that the interactions between neuronal processes and MWCNTs in the third dimension promote successful transfer of information between separated CNS explants. Although 3D CNF scaffolds appear beneficial to neuronal function in vitro, their biointeraction in vivo has never been tested. The ultimate potential of any new multifunctional device with microfeatures and nanofeatures for biomedical applications resides in its integration with the biological milieu in vivo. An assessment of the microenvironment responses to 3D CNF implants should entail evaluating the surrounding distribution patterns and the infiltration of microglia together with astrocyte aggregation at the scaffold interface (14, 31, 32). In addition, a recent report has demonstrated the ability of graphene-based implants to attract migrating neuroblasts (14). Thus, to reduce the current gap in the knowledge of 3D CNF performance in the CNS, we designed a study to observe the in vivo biocompatibility of 3D CNF. Before any larger assessment of the functional outcomes of 3D CNF was implanted into, for example, the lesioned spinal cord, we felt it pertinent to report here the performance of 3D CNF when challenged by a physiological environment. We implanted pure 3D CNF scaffolds in the brains of four adult male Wistar rats using material samples with a relatively large lateral dimension when compared to typical neuroprosthetic devices, such as electrodes (33). These scaffolds were completely implanted into the visual cortex and the animals were sacrificed at 4 weeks after implantation to assess the in vivo response to the material. We focused our experimental group at the 4-week time point, because this is the optimal time to explore the persistence of inflammatory states and glial activation [in agreement with similar studies (34–36)]. In addition, we performed an exploratory longitudinal study with five animals sacrificed at different time points to confirm tissue response progression.

Figure 4 reports the tissue reaction to the implanted scaffold. Notably, when immunolabeled for glial fibrillary acidic protein (GFAP), the GFAP fluorescence intensity profile peak in the tissue immediately surrounding the scaffold was limited, at 4 weeks, within a relatively restricted reactive area (<20  $\mu\text{m}$ ; Fig. 4, A to C) (14) when compared to other artificial implants (~60 to 100  $\mu\text{m}$ ; highlighted by the dashed line in Fig. 4A) (37, 38). Although a notable astrocytic response, the limited thickness of the GFAP-reactive region suggests that this formation may not be inhibitory to successful long-term integration of the material into the tissue (37–41). Ionized calcium-binding adapter protein 1 (Iba1)-positive microglial reactivity in the area immediately surrounding the tissue was low across all animals (Fig. 4D). Iba1-positive microglia were found to have effectively infiltrated the scaffold (Fig. 4E) but did not form a significant scar-like formation at the implant edge (Fig. 4D), and we never detected any sign of progressive cavitation usually accompanying large inflammation processes.

The tissue reaction detected is promising, suggesting implant integration with the tissue. We further investigated whether the astrocyte and microglial localization within and around the 3D CNF represented a barrier for neurons to invade the construct (42, 43). In 79% of horizontal sections tested (19 of 24 horizontal slices), we detected  $\beta$ -tubulin III-positive cells (Fig. 4G, top) progressively infiltrating the implanted 3D CNF, coexisting but never colocalizing with either Iba1-positive cells (Fig. 4G, top left) inside the structure or GFAP-positive cells located at the implant edges (not shown). We cannot exclude the fact that some  $\beta$ -tubulin III-positive processes penetrate the implant and embrace unlabeled cell somata. To clarify this issue, we used a specific neuronal

marker. Further supporting the presence of neuronal cells is the finding of neuronal nuclear antigen (NeuN)-positive cells within the scaffold (Fig. 4G, bottom). Because of the scaffold infiltration that improves stiffness before implantation (see Materials and Methods), we discount the fact that these are neurons that became trapped in the implant during insertion. These cells could be newly generated neurons migrating as a result of injury-mediated mechanisms (14, 44, 45). The presence of neuronal cells within the implant is surprising but agrees with a recent report describing migrating neuroblasts localized in implanted graphene-based scaffolds even at a certain distance from their source (14). Further studies are required to solve this issue beyond the current investigation; however, this evidence supports the notion that the immune response to the scaffold at 4 weeks does not prevent the infiltration of neuronal populations.

It is tempting to speculate that the presence of microglia localized inside the 3D CNF may also represent a reaction beneficial to tissue repair (14, 46, 47). Certainly, the tissue reaction to the implant is complex, but our evidence regarding scar formation and neuronal infiltration supports the hypothesis that the material is capable of integrating into the surrounding neural tissue. We observed no gross differences in tissue anatomy in other brain regions removed from the immediate implant area, including the contralateral hemisphere (insets to Fig. 4, B, E, and H).

In addition to the four animals analyzed at 4 weeks after implantation, we were interested in the tissue response over time. Thus, in an exploratory longitudinal study, we assessed the long-term immune reaction surrounding the implanted CNF scaffold over time in additional animals (each sacrificed at five different time points). The animals were sacrificed immediately following implantation (0 weeks, as an indicator of implant procedure damage) and at 1, 2, 4, and 8 weeks after implantation. After 8 weeks, the peak of the GFAP-reactive area is even smaller (<10  $\mu\text{m}$ ; fig. S5A) compared with after 4 weeks, with several areas completely devoid of GFAP reactivity. Figure S5B illustrates samples of the regions of interest (ROIs) used for analysis to demonstrate how the astrocyte reactivity in the adjacent tissue changes over time. Microglia reactivity was found to be increased at 1 week after implantation in the area immediately surrounding the 3D CNF, which is likely due to the initial inflammatory response to the compressive tissue damage induced by introducing the material itself (33, 37, 40, 41). However, 2 weeks after implantation and up until 8 weeks, the Iba1 reaction surrounding the implant progressively declined toward normal values and became sparse close to the 3D CNF (fig. S5, C and D). Although the reported longitudinal data in vivo are indeed preliminary, we suggest that, in a more complete study, adverse effects to CNS-implanted 3D CNF are likely to be limited.

Here, we tested the biointegration of implanted 3D CNF and animal survival within the time frame generally accepted in biocompatibility assessments (4 to 8 weeks) (14, 34–36, 48, 49). The general animal conditions (see the Supplementary Materials), together with the subsequent tissue histology, support the good postimplantation survival of all tested 3D CNF subjects. We observed no substantial effects of scaffold implantation on general animal behavior and/or well-being at any time point. There is no reason to suspect that the health of implanted animals beyond 8 weeks would be compromised; however, because of the well-known long-term stability in the biological milieu of carbon nanotube structures (50), the long-term survival (beyond 8 weeks) of implanted animals and the resulting implications of scaffold presence in the CNS will require additional studies. The in vivo monitoring of long-term responses to implantable neural technologies

**Fig. 4. Tissue reaction to CNF scaffolds implanted into the adult rat visual cortex.** (A) GFAP fluorescence intensity profile as a function of the distance from the edge of the implant in brain tissue. The average GFAP intensity at 4 weeks after implantation peaked at 10  $\mu\text{m}$  from the implant edge on average and gradually decreased away from the implant edge. (B) GFAP-positive cells (green) are found surrounding the implant and within the material; boxed areas indicate high-magnification images shown in (C); inset: contralateral hemisphere used as a control. (C) High magnification of GFAP reactivity at the implant edge demonstrates the minimal and irregular cellular localization around the scaffold. (D) Iba1-positive area (as a fraction of total tissue area in the ROI) varies from  $0.08 \pm 0.05$  to  $0.17 \pm 0.05$  (roughly 8 to 17% of the tissue area) at 4 weeks after implantation, with an average of  $0.13 \pm 0.08$ . (E) Iba1-positive cells (red) are dispersed consistently throughout the tissue and within the material; boxed areas indicate high-magnification images shown in (F); inset: contralateral hemisphere used as a control. (F) High-magnification images of the Iba1 reactivity demonstrate no obvious border at the implant edge to indicate scar formation. (G) Top left:  $\beta$ -Tubulin III-positive cells (red; DAPI, blue) within the scaffold and surrounded by Iba1-positive microglia (green) (note the absence of colocalization). Top right:  $\beta$ -Tubulin III-positive cells (red; DAPI, blue) within the scaffold from another animal, suggestive of the fact that neuronal process infiltration may be consistent at 4 weeks after implantation. Bottom: NeuN-positive cells (green; DAPI, blue) within the scaffold and two different areas are shown. (H) NeuN-positive cells (green; DAPI, blue) within the contralateral hemisphere; inset: high magnification of NeuN-positive cells. Scale bars, 200  $\mu\text{m}$  (B and E), 50  $\mu\text{m}$  (C and F), 20  $\mu\text{m}$  (G), and 100 and 10  $\mu\text{m}$  (inset) (H).

presents unique challenges and represents an active area of research (51). Our study identifies artificial, conductive (52) 3D CNF constructs as suitable structures to guide neuronal fiber reconstruction and signal transmission in vitro. In vivo, the low tissue reaction induced by the implantation of unmodified MWCNT microsystems provides a crucial factor to the further design of miniaturized platforms based on entirely new materials and concepts toward functionally integrated interfaces (1–4). Understanding the potential of nanomaterial-based conductive scaffolds may promote the design of novel interventions (14, 53) where the scaffold in itself is critical to the success of the implant.

## MATERIALS AND METHODS

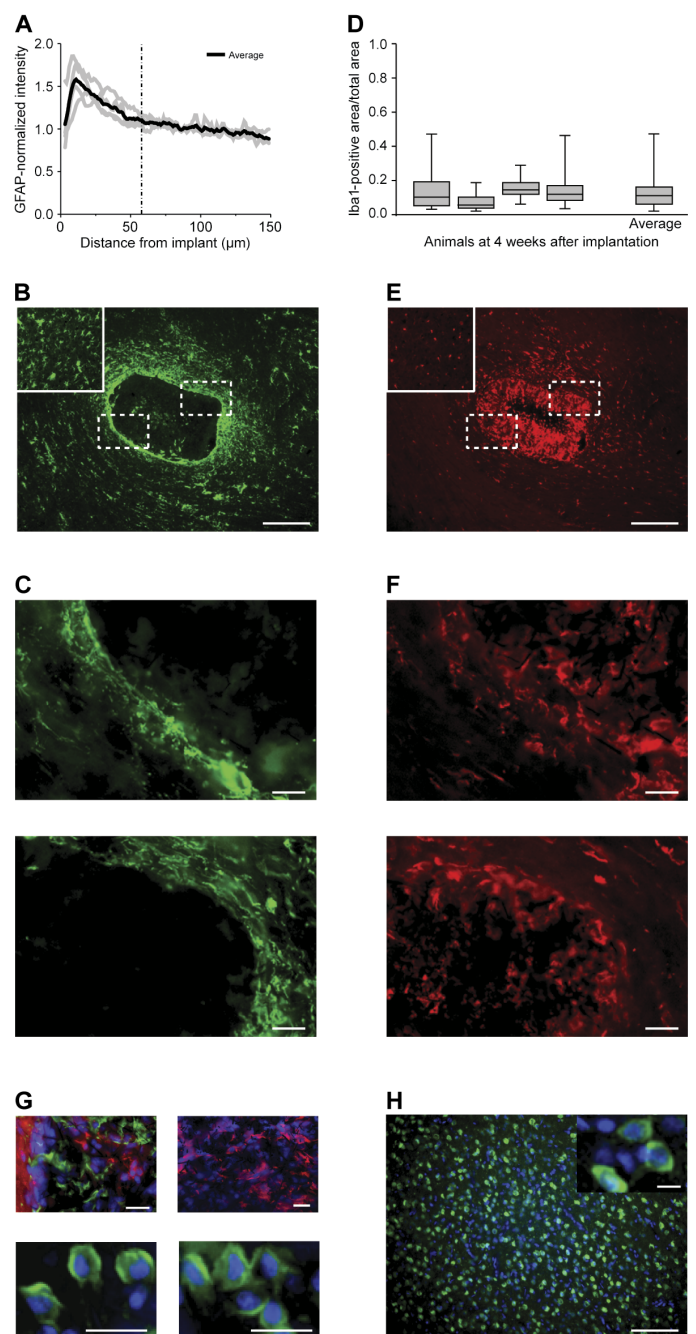
### 3D CNFs, PDMS scaffolds, and 2D MWCNTs

3D CNFs were obtained from the laboratory of M.D.C. as previously reported (52, 54, 55) (see the Supplementary Materials for details). The bulky 3D scaffolds were cut into thin square slices (lateral size, 3 mm  $\times$  4 mm; thickness, 250 to 400  $\mu\text{m}$ ) and then secured on standard glass coverslips (Kindler) by PDMS (Sylgard 184 silicone elastomer, Dow Corning) cured at 150°C for 15 min. Thereafter, substrates were cleaned under low-pressure air plasma for 5 min (PDC-32G Plasma Cleaner, Harrick Plasma) and ultraviolet (UV)–sterilized for 20 min before use.

PDMS scaffolds are 3D, self-standing, porous microsponges fabricated as described by Bosi *et al.* (28). 2D MWCNT supports were obtained as previously described by Fabbro *et al.* (8).

### Organotypic spinal explant preparation

Organotypic cultures were obtained from spinal cords of E12 embryonic mouse (C57BL) as previously reported (8, 21, 26) (see the Supplementary Materials for details). To ensure homogeneous experimental conditions between the two analyzed populations (Control and 3D CNF double-cultured spinal slice pairs), pairs of organotypic spinal explants with interslice distance (measured between the center of the two explants by



bright-field imaging) exceeding the 0.8- to 2.5-mm range were discarded for electrophysiological and immunofluorescence experiments.

### Electrophysiological recordings

All electrophysiological experiments were performed at room temperature as previously described (8, 20, 21). The synchrony between the bursting activities of the two explants in each pair was assessed by computing the Pearson CCF between the two voltage time series (see the Supplementary Materials for details).

### Immunofluorescence labeling and confocal imaging of spinal slice explants

Images of labeled organotypic cultures were acquired using a Nikon C2 or a Leica DMIRE2 confocal microscope, both equipped with argon/krypton, helium/neon, and UV lasers. Images were acquired with a 20×, 40×, or 63× oil objective (numerical aperture, 1.4) using oil-mounting medium (1.515 refractive index). Analysis and 3D reconstruction of the image Z stack were accomplished using NIS-Elements AR (Nikon), Volocity (PerkinElmer), and Fiji (<http://fiji.sc/Fiji>) software.

To measure the alignment of outgrowing fibers, we quantified their relative orientation based on fiber directionality analysis (23): When the dispersion of the mean fiber's direction was lower than 15°, we defined them as "oriented," whereas when it was higher than 15°, we defined them as "random." Briefly, the mean fiber's direction and relative dispersion were computed from 640 μm × 640 μm confocal images (12 and 15 randomly sampled images,  $n = 4$  and  $n = 5$ , for Control and 3D CNF, respectively) where neuronal processes were visualized by β-tubulin III immunofluorescence (fig. S4). The analysis was carried out using the Directionality plugin of Fiji software inferring the preferred orientation of "structures" present in the input image. Fiber orientation was calculated via a Fourier component analysis (23).

A histogram that indicates the amount of structures displaying a given direction was computed, and a Gaussian fitting was applied (see Fig. 1C and fig. S4). Images with a completely isotropic content will result into a flat histogram, leading to a high dispersion value of the Gaussian fitting, whereas images with a clear alignment (for example, bundles of fibers with preferred orientations) will present a narrow peak at that orientation in the relative histogram and will be characterized by a smaller dispersion value. The dispersion value is the SD of the Gaussian fit (see the Supplementary Materials for additional details on image analysis).

### Brain tissue implantation with 3D CNF

All surgical procedures were performed on anesthetized male Wistar rats (Harlan Laboratories;  $n = 9$ ) aged 3 to 6 months and weighing 450 to 550 g. The implant consisted of a sharp-pointed cylinder (~2 mm in length and  $0.5 \pm 0.2$  mm in diameter) carved out of a larger 3D CNF scaffold and mounted on an electrode holder (ZIF-Clip, Tucker-Davis Technologies). Implant stiffness was increased via polyethylene glycol (PEG) scaffold permeation before the carving procedure to facilitate the insertion of the material into the brain tissue. The PEG-stiffened 3D CNF scaffold was inserted into the visual cortex. For the study of biocompatibility (data reported in Fig. 4),  $n = 4$  animals were sacrificed at 4 weeks after implantation. For the exploratory longitudinal study aimed at investigating the response over time,  $n = 5$  animals were sacrificed at 0, 1, 2, 4, and 8 weeks after implantation (data reported in fig. S5; see the Supplementary Materials for details).

### Brain tissue preparation, immunohistochemistry, image acquisition, and analysis

Animals were anesthetized with chloral hydrate and then sacrificed via transcardial perfusion with 0.1 M phosphate-buffered saline (PBS) followed by 4% formaldehyde (prepared from fresh paraformaldehyde) in PBS. Brains were removed, postfixed, embedded in optimal cutting temperature compound (Tissue-Tek), and cryosectioned horizontally as 25-μm-thick sections. After immunohistochemistry, sections were mounted on glass coverslips using Vectashield Hard Mounting Medium (Vector Laboratories). We measured the brain tissue reaction at 4 weeks after implantation using GFAP for astrocytes and Iba1 for microglia.

We also labeled the tissue sections for neurons using β-tubulin III and a marker for NeuN. At 4 weeks after implantation, the mean-normalized GFAP intensity in the region up to 150 μm from the edge of the implant was  $1.11 \pm 0.19$ , with an average peak of fluorescence intensity (as an indicator of the maximum localization of GFAP-positive astrocytes) of 25 μm from the implant edge. In the four animals at this time point, this peak ranged from 8 to 16 μm from the edge of the implant, which is a relatively tight window. As a fraction of the total tissue area, normalized to the reactivity in the contralateral hemisphere, the average Iba1-reactive area for these animals was  $0.13 \pm 0.08$ . This indicates that, on average, about 13% of the total tissue area within 500 μm surrounding the implant was composed of Iba1-positive microglia (see the Supplementary Materials for details).

### Scanning electron microscopy

3D CNF morphology before and after culturing was qualitatively assessed through SEM. Images were acquired through collecting secondary electrons on a Gemini SUPRA 40 SEM (Carl Zeiss NTS GmbH). Before imaging, samples were gold-metalized on a metal sputter coater.

### Mechanical characterization

The mechanical properties of 3D CNF scaffolds were evaluated via uniaxial microcompression tests conducted on a Galdabini SUN 500 apparatus. Tests were performed in air at room temperature. Elastic data were determined by calculating the initial linear slope of the stress-strain curve (see the Supplementary Materials for details).

### Statistics

All values from samples subjected to the same experimental protocols were pooled together and expressed as means  $\pm$  SD, with  $n$  being the number of cultures, unless otherwise specified. Where not otherwise indicated, statistically significant differences between data sets were assessed by Student's  $t$  test (after validation of variance homogeneity by Levene's test) for parametric data and by the Mann-Whitney  $U$  test for nonparametric data. For estimating significantly synchronous slices in the two groups and for the percentage of oriented fields, we performed a homogeneity test with the  $\chi^2$  method. One-way ANOVA was used to determine significance when multiple groups were compared (for example, directionality dispersion), and Fisher's least significant difference was used to determine significance post hoc. Statistical significance was determined at  $P < 0.05$ .

### Ethical statement

All animal procedures were conducted in accordance with the National Institutes of Health and with international and institutional standards for the care and use of animals in research, and after consulting with a veterinarian. All experiments were performed in accordance with European Union (EU) guidelines (2010/63/UE) and Italian law (decree 26/14) and were approved by the local authority veterinary service and by our institutional (SISSA-ISAS) ethical committee. All efforts to minimize animal suffering and to reduce the number of animals used were made. Animal use was approved by the Italian Ministry of Health, in agreement with the EU Recommendation 2007/526/CE ([http://eur-lex.europa.eu/legal-content/EN/TXT/?uri=uriserv:OJ.L\\_.2007.197.01.0001.01.ENG&toc=OJ:L:2007:197:TOC](http://eur-lex.europa.eu/legal-content/EN/TXT/?uri=uriserv:OJ.L_.2007.197.01.0001.01.ENG&toc=OJ:L:2007:197:TOC)).

### SUPPLEMENTARY MATERIALS

Supplementary material for this article is available at <http://advances.sciencemag.org/cgi/content/full/2/7/e1600087/DC1>  
Supplementary Materials and Methods

fig. S1. Illustration of the permutation test to assess the statistical significance of the synchrony between the bursting activities of two cocultured explants.

fig. S2. Organotypic spinal slices cultured on 2D MWCNT substrates and on 3D-PDMS scaffolds.

fig. S3. Extracellular voltage transients represent evoked or spontaneous synaptic, action potential-mediated activity.

fig. S4. Directionality analysis of spinal neuronal process outgrowth.

fig. S5. Immune reaction over time to CNF scaffolds implanted into the adult rat visual cortex as a pilot study.

References (56–61)

## REFERENCES AND NOTES

- B. Tian, J. Liu, T. Dvir, L. Jin, J. H. Tsui, Q. Qing, Z. Suo, R. Langer, D. S. Kohane, C. M. Lieber, Macroporous nanowire nanoelectronic scaffolds for synthetic tissues. *Nat. Mater.* **11**, 986–994 (2012).
- D. K. Cullen, J. A. Wolf, D. H. Smith, B. J. Pfister, Neural tissue engineering for neuroregeneration and hybridized interface microsystems in vivo (part 2). *Crit. Rev. Biomed. Eng.* **39**, 241–259 (2011).
- J. L. Collinger, S. Foldes, T. M. Bruns, B. Wodlinger, R. Gaunt, D. J. Weber, Neuroprosthetic technology for individuals with spinal cord injury. *J. Spinal Cord Med.* **36**, 258–272 (2013).
- A. Jackson, J. B. Zimmermann, Neural interfaces for the brain and spinal cord—Restoring motor function. *Nat. Rev. Neurol.* **8**, 690–699 (2012).
- N. A. Kotov, J. O. Winter, I. P. Clements, E. Jan, B. P. Timko, S. Campidelli, S. Pathak, A. Mazzatenta, C. M. Lieber, M. Prato, R. V. Bellamkonda, G. A. Silva, N. W. S. Kam, F. Patolsky, L. Ballerini, Nanomaterials for neural interfaces. *Adv. Mater.* **21**, 3970–4004 (2009).
- G. Cellot, E. Cilia, S. Cipollone, V. Rancic, A. Supacane, S. Giordani, L. Gambazzi, H. Markram, M. Grandolfo, D. Scaini, F. Gelain, L. Casalis, M. Prato, M. Giugliano, L. Ballerini, Carbon nanotubes might improve neuronal performance by favouring electrical shortcuts. *Nat. Nanotechnol.* **4**, 126–133 (2009).
- G. Cellot, F. M. Toma, Z. K. Varley, J. Laishram, A. Villari, M. Quintana, S. Cipollone, M. Prato, L. Ballerini, Carbon nanotube scaffolds tune synaptic strength in cultured neural circuits: Novel frontiers in nanomaterial–tissue interactions. *J. Neurosci.* **31**, 12945–12953 (2011).
- A. Fabbro, A. Villari, J. Laishram, D. Scaini, F. M. Toma, A. Turco, M. Prato, L. Ballerini, Spinal cord explants use carbon nanotube interfaces to enhance neurite outgrowth and to fortify synaptic inputs. *ACS Nano* **6**, 2041–2055 (2012).
- A. Fabbro, M. Prato, L. Ballerini, Carbon nanotubes in neuroregeneration and repair. *Adv. Drug Deliv. Rev.* **65**, 2034–2044 (2013).
- V. Lovat, F. Pantarotto, L. Lagostena, B. Cacciari, M. Grandolfo, M. Righi, G. Spalluto, M. Prato, L. Ballerini, Carbon nanotube substrates boost neuronal electrical signaling. *Nano Lett.* **5**, 1107–1110 (2005).
- A. Mazzatenta, M. Giugliano, S. Campidelli, L. Gambazzi, L. Businaro, H. Markram, M. Prato, L. Ballerini, Interfacing neurons with carbon nanotubes: Electrical signal transfer and synaptic stimulation in cultured brain circuits. *J. Neurosci.* **27**, 6931–6936 (2007).
- H. Hu, Y. Ni, V. Montana, R. C. Haddon, V. Parpura, Chemically functionalized carbon nanotubes as substrates for neuronal growth. *Nano Lett.* **4**, 507–511 (2004).
- M. F. L. De Volder, S. H. Tawfik, R. H. Baughman, A. J. Hart, Carbon nanotubes: Present and future commercial applications. *Science* **339**, 535–539 (2013).
- K. Zhou, S. Motamed, G. A. Thouas, C. C. Bernard, D. Li, H. C. Parkington, H. A. Coleman, D. I. Finkelstein, J. S. Forsythe, Graphene functionalized scaffolds reduce the inflammatory response and supports endogenous neuroblast migration when implanted in the adult brain. *PLOS One* **11**, e0151589 (2016).
- B. Zhu, S.-C. Luo, H. Zhao, H.-A. Lin, J. Sekine, A. Nakao, C. Chen, Y. Yamashita, H.-h. Yu, Large enhancement in neurite outgrowth on a cell membrane-mimicking conducting polymer. *Nat. Commun.* **5**, 4523 (2014).
- T. Dvir, B. P. Timko, D. S. Kohane, R. Langer, Nanotechnological strategies for engineering complex tissues. *Nat. Nanotechnol.* **6**, 13–22 (2011).
- J. A. Roman, T. L. Niedzielko, R. C. Haddon, V. Parpura, C. L. Floyd, Single-walled carbon nanotubes chemically functionalized with polyethylene glycol promote tissue repair in a rat model of spinal cord injury. *J. Neurotrauma* **28**, 2349–2362 (2011).
- M. Heidemann, J. Streit, A. Tschertner, Functional regeneration of intraspinal connections in a new in vitro model. *Neuroscience* **262**, 40–52 (2014).
- J. Gerardo-Nava, D. Hodde, I. Katona, A. Bozkurt, T. Grehl, H. W. M. Steinbusch, J. Weis, G. A. Brook, Spinal cord organotypic slice cultures for the study of regenerating motor axon interactions with 3D scaffolds. *Biomaterials* **35**, 4288–4296 (2014).
- L. Ballerini, M. Galante, M. Grandolfo, A. Nistri, Generation of rhythmic patterns of activity by ventral interneurons in rat organotypic spinal slice culture. *J. Physiol.* **517**, 459–475 (1999).
- D. Avossa, M. D. Rosato-Siri, F. Mazzarol, L. Ballerini, Spinal circuits formation: A study of developmentally regulated markers in organotypic cultures of embryonic mouse spinal cord. *Neuroscience* **122**, 391–405 (2003).
- G. Courtine, B. Song, R. R. Roy, H. Zhong, J. E. Herrmann, Y. Ao, J. Qi, V. R. Edgerton, M. V. Sofroniew, Recovery of supraspinal control of stepping via indirect propriospinal relay connections after spinal cord injury. *Nat. Med.* **14**, 69–74 (2008).
- Z. Q. Liu, Scale space approach to directional analysis of images. *Appl. Opt.* **30**, 1369–1373 (1991).
- J. Streit, Regular oscillations of synaptic activity in spinal networks in vitro. *J. Neurophysiol.* **70**, 871–878 (1993).
- M. Galante, A. Nistri, L. Ballerini, Opposite changes in synaptic activity of organotypic rat spinal cord cultures after chronic block of AMPA/kainate or glycine and GABA<sub>A</sub> receptors. *J. Physiol.* **523**, 639–651 (2000).
- F. Furlan, G. Taccola, M. Grandolfo, L. Guasti, A. Arcangeli, A. Nistri, L. Ballerini, ERG conductance expression modulates the excitability of ventral horn GABAergic interneurons that control rhythmic oscillations in the developing mouse spinal cord. *J. Neurosci.* **27**, 919–928 (2007).
- E. Bracci, L. Ballerini, A. Nistri, Localization of rhythmogenic networks responsible for spontaneous bursts induced by strychnine and bicuculline in the rat isolated spinal cord. *J. Neurosci.* **16**, 7063–7076 (1996).
- S. Bosi, R. Rauti, J. Laishram, A. Turco, D. Lonardoni, T. Nieuw, M. Prato, D. Scaini, L. Ballerini, From 2D to 3D: Novel nanostructured scaffolds to investigate signaling in reconstructed neuronal networks. *Sci. Rep.* **5**, 9562 (2015).
- E. Bracci, M. Beato, A. Nistri, Afferent inputs modulate the activity of a rhythmic burst generator in the rat disinhibited spinal cord in vitro. *J. Neurophysiol.* **77**, 3157–3167 (1997).
- M. M. Stevens, J. H. George, Exploring and engineering the cell surface interface. *Science* **310**, 1135–1138 (2005).
- E. R. Aurand, J. Wagner, C. Lanning, K. B. Bjugstad, Building biocompatible hydrogels for tissue engineering of the brain and spinal cord. *J. Funct. Biomater.* **3**, 839–863 (2012).
- E. Fournier, C. Passirani, C. N. Montero-Menei, J. P. Benoit, Biocompatibility of implantable synthetic polymeric drug carriers: Focus on brain biocompatibility. *Biomaterials* **24**, 3311–3331 (2003).
- J. Thelin, H. Jörmell, E. Psouni, M. Garwicz, J. Schouenborg, N. Danielsen, C. E. Linsmeier, Implant size and fixation mode strongly influence tissue reactions in the CNS. *PLOS One* **6**, e16267 (2011).
- R. Biran, M. D. Noble, P. A. Tresco, Directed nerve outgrowth is enhanced by engineered glial substrates. *Exp. Neurol.* **184**, 141–152 (2003).
- J. P. Seymour, D. R. Kipke, Neural probe design for reduced tissue encapsulation in CNS. *Biomaterials* **28**, 3594–3607 (2007).
- J. N. Turner, W. Shain, D. H. Szarowski, M. Andersen, S. Martins, M. Isaacson, H. Craighead, Cerebral astrocyte response to micromachined silicon implants. *Exp. Neurol.* **156**, 33–49 (1999).
- Y. Zhong, R. V. Bellamkonda, Dexamethasone-coated neural probes elicit attenuated inflammatory response and neuronal loss compared to uncoated neural probes. *Brain Res.* **1148**, 15–27 (2007).
- B. D. Winslow, M. B. Christensen, W.-K. Yang, F. Solzbacher, P. A. Tresco, A comparison of the tissue response to chronically implanted Parylene-C-coated and uncoated planar silicon microelectrode arrays in rat cortex. *Biomaterials* **31**, 9163–9172 (2010).
- W. He, G. C. McConnell, R. V. Bellamkonda, Nanoscale laminin coating modulates cortical scarring response around implanted silicon microelectrode arrays. *J. Neural Eng.* **3**, 316–326 (2006).
- G. Lind, C. E. Lindmeier, J. Schouenborg, The density difference between tissue and neural probes is a key factor for glial scarring. *Sci. Rep.* **3**, 2942 (2013).
- Y.-T. Kim, R. W. Hitchcock, M. J. Bridge, P. A. Tresco, Chronic response of adult rat brain tissue to implants anchored to the skull. *Biomaterials* **25**, 2229–2237 (2004).
- C. J. Rivet, K. Zhou, R. J. Gilbert, D. I. Finkelstein, J. S. Forsythe, Cell infiltration into a 3D electrospun fiber and hydrogel hybrid scaffold implanted in the brain. *Biomatter* **5**, e1005527 (2015).
- D. R. Nisbet, A. E. Rodda, M. K. Horne, J. S. Forsythe, D. I. Finkelstein, Neurite infiltration and cellular response to electrospun polycaprolactone scaffolds implanted into the brain. *Biomaterials* **30**, 4573–4580 (2009).
- H. T. Ghashghaei, C. Lai, E. S. Anton, Neuronal migration in the adult brain: Are we there yet? *Nat. Rev. Neurosci.* **8**, 141–151 (2007).
- A. M. Osman, M. J. Porritt, M. Nilsson, H. G. Kuhn, Long-term stimulation of neural progenitor cell migration after cortical ischemia in mice. *Stroke* **42**, 3559–3565 (2011).
- H. Neumann, M. R. Kotter, R. J. M. Franklin, Debris clearance by microglia: An essential link between degeneration and regeneration. *Brain* **132**, 288–295 (2009).
- U.-K. Hanisch, H. Kettenmann, Microglia: Active sensor and versatile effector cells in the normal and pathologic brain. *Nat. Neurosci.* **10**, 1387–1394 (2007).
- I. R. Mineev, P. Musienko, A. Hirsch, Q. Barraud, N. Wenger, E. M. Moraud, J. Gandar, M. Capogrosso, T. Milekovic, L. Asboth, R. F. Torres, N. Vachicouras, Q. Liu, N. Pavlova,

- S. Duis, A. Larmagnac, J. Vörös, S. Micera, Z. Suo, G. Courtine, S. P. Lacour, *Biomaterials*. Electronic dura mater for long-term multimodal neural interfaces. *Science* **347**, 159–163 (2015).
49. S. De Faveri, E. Maggolini, E. Miele, F. De Angelis, F. Cesca, F. Benfenati, L. Fadiga, Bio-inspired hybrid microelectrodes: A hybrid solution to improve long-term performance of chronic intracortical implants. *Front. Neuroeng.* **7**, 7 (2014).
50. A. Nunes, C. Bussy, L. Gherardini, M. Meneghetti, M. A. Herrero, A. Bianco, M. Prato, T. Pizzorusso, K. T. Al-Jamal, K. Kostarelos, In vivo degradation of functionalized carbon nanotubes after stereotactic administration in the brain cortex. *Nanomedicine* **7**, 1485–1494 (2012).
51. T. D. Y. Kozai, J. R. Eles, A. L. Vazquez, X. T. Cui, Two-photon imaging of chronically implanted neural electrodes: Sealing methods and new insights. *J. Neurosci. Methods* **258**, 46–55 (2016).
52. L. Camilli, C. Pisani, M. Passacantando, V. Grossi, M. Scarselli, P. Castrucci, M. De Crescenzi, Pressure-dependent electrical conductivity of freestanding three-dimensional carbon nanotube network. *Appl. Phys. Lett.* **102**, 183117 (2013).
53. M. E. Spira, A. Hai, Multi-electrode array technologies for neuroscience and cardiology. *Nat. Nanotechnol.* **8**, 83–94 (2013).
54. L. Camilli, C. Pisani, E. Gautron, M. Scarselli, P. Castrucci, F. D'Orazio, M. Passacantando, D. Moscone, M. De Crescenzi, A three-dimensional carbon nanotube network for water treatment. *Nanotechnology* **25**, 065071 (2014).
55. X. Gui, J. Wei, K. Wang, A. Cao, H. Zhu, Y. Jia, Q. Shu, D. Wu, Carbon nanotube sponges. *Adv. Mater.* **22**, 617–621 (2010).
56. W. J. Tyler, The mechanobiology of brain function. *Nat. Rev. Neurosci.* **13**, 867–878 (2012).
57. A. Tscherter, M. O. Heuschkel, P. Renaud, J. Streit, Spatiotemporal characterization of rhythmic activity in rat spinal cord slice cultures. *Eur. J. Neurosci.* **14**, 179–190 (2001).
58. M. D. Rosato-Siri, D. Zoccolan, F. Furlan, L. Ballerini, Interneurone bursts are spontaneously associated with muscle contractions only during early phases of mouse spinal network development: A study in organotypic cultures. *Eur. J. Neurosci.* **20**, 2697–2710 (2004).
59. K. B. Bjugstad, K. Lampe, D. S. Kern, M. Mahoney, Biocompatibility of poly(ethylene glycol)-based hydrogels in the brain: An analysis of the glial response across space and time. *J. Biomed. Mater. Res. A* **95**, 79–91 (2010).
60. K. B. Bjugstad, D. E. Redmond Jr., K. J. Lampe, D. S. Kern, J. R. Sladek Jr., M. J. Mahoney, Biocompatibility of PEG-based hydrogels in primate brain. *Cell Transplant.* **17**, 409–415 (2008).
61. G. Paxinos, C. Watson, *The Rat Brain in Stereotaxic Coordinates* (Elsevier Academic Press, San Diego, 2005).

**Acknowledgments:** We are grateful to M. Gandolfo and D. Cojoc for supervising the confocal image analysis and reconstruction, G. Turco for characterizing the material compressibility, and L. Camilli for the pioneering work on the growth of MWCNT networks. Istituto Officina dei Materiali – Tecnologie Avanzate e Nano Scienza (Trieste) is also acknowledged for SEM assistance. **Funding:** We acknowledge financial support from EOARD no. FA9550-14-1-0047 to M.D.C. and NEUROSCAFFOLDS-FP7-NMP-604263, CARBONANOBIDGE-ERC-2008-227135, and PRIN-MIUR no. 2012MYESZW to M.P. and L.B. **Author contributions:** S.U. and A.F. performed electrophysiology, immunofluorescence, confocal experiments, and all experimental analysis on slice cultures; M.M. and E.R.A. designed and performed histology, immunofluorescence confocal microscopy, and analysis on brain sections; J.L. performed immunofluorescence confocal microscopy; F.B.R. and D.Z. designed and performed the neurosurgery experiments; A.A. and D.Z. designed and implemented the statistical analysis to assess the synchrony of the bursting activity; D.S. designed the experiments, designed and contributed to the experimental analysis of data, and performed material preparation, measurements, and SEM; M.S. and M.D.C. provided the material; S.B. contributed to material analysis and preparation; M.P. and L.B. conceived the study and provided funding; L.B. designed the experiments and designed and contributed to the analysis of data; and E.R.A. and L.B. wrote the article. All authors discussed the results and commented on the article. **Competing interests:** The authors declare that they have no competing interests. **Data and materials availability:** All data needed to evaluate the conclusions in the paper are present in the paper and/or the Supplementary Materials. Additional data related to this paper may be requested from the authors.

Submitted 18 January 2016

Accepted 22 June 2016

Published 15 July 2016

10.1126/sciadv.1600087

**Citation:** S. Usmani, E. R. Aurand, M. Medelin, A. Fabbro, D. Scaini, J. Laishram, F. B. Rosselli, A. Ansuini, D. Zoccolan, M. Scarselli, M. De Crescenzi, S. Bosi, M. Prato, L. Ballerini, 3D meshes of carbon nanotubes guide functional reconnection of segregated spinal explants. *Sci. Adv.* **2**, e1600087 (2016).

This article is published under a Creative Commons license. The specific license under which this article is published is noted on the first page.

For articles published under [CC BY](#) licenses, you may freely distribute, adapt, or reuse the article, including for commercial purposes, provided you give proper attribution.

For articles published under [CC BY-NC](#) licenses, you may distribute, adapt, or reuse the article for non-commercial purposes. Commercial use requires prior permission from the American Association for the Advancement of Science (AAAS). You may request permission by clicking [here](#).

***The following resources related to this article are available online at <http://advances.sciencemag.org>. (This information is current as of July 18, 2016):***

**Updated information and services**, including high-resolution figures, can be found in the online version of this article at:

<http://advances.sciencemag.org/content/2/7/e1600087.full>

**Supporting Online Material** can be found at:

<http://advances.sciencemag.org/content/suppl/2016/07/11/2.7.e1600087.DC1>

This article **cites 60 articles**, 11 of which you can access for free at:

<http://advances.sciencemag.org/content/2/7/e1600087#BIBL>

*Science Advances* (ISSN 2375-2548) publishes new articles weekly. The journal is published by the American Association for the Advancement of Science (AAAS), 1200 New York Avenue NW, Washington, DC 20005. Copyright is held by the Authors unless stated otherwise. AAAS is the exclusive licensee. The title *Science Advances* is a registered trademark of AAAS